GEOPHYSICAL TRANSACTIONS 1994
Vol. 39. No. 4. pp. 263-288

THREE DIMENSIONAL SEISMIC MODELLING BY FINITE ELEMENT CONDENSATION TECHNIQUE

Sankar Kumar NATH*, Swapan MAJUMDAR** and Saradindu SENGUPTA*

A seismic section represents a two-dimensional picture of reflected waves which propagate in three-dimensional space. Present day computational facilities enable the seismic responses of the earth to be investigated more accurately by setting up wave equations based on 3-D models. Various numerical modelling techniques are available to simulate seismic responses in 3-D, such as the finite element method. Unlike other schemes, this method needs an efficient networking of computers to handle multifold data. The purpose of this paper is to present an efficient and economical finite element algorithm for modelling seismic responses in 3-D, keeping in view (i) the reduction of memory and storage requirements, (ii) the suitability for multiple processors and mini-computers. The degree of freedom is reduced by introducing hierarchical modes in the form of Legendre's polynomials to achieve kinematic condensation of the global matrices. The normal incidence synthetic seismograms computed along six profiles over a 3-D dome model along with the snapshots and the isotime map given in the paper, prove the validity of the proposed algorithm.

Keyword: seismic section, finite element method, hierarchical modes, kinematic condensation, normal incidence synthetic seismograms

1. Introduction

Numerical modelling of seismic wave propagation has become an important component of seismic prospecting. Probably the most common applicaton of such modelling is in the context of interpreting seismic data. Generally geophysical data are interpreted and translated into a subsurface geological

* Dept. of Geology & Geophysics, Indian Institute of Technology, Kharagpur 721302, West Bengal, India

** Dept. of Civil Engineering, Indian Institute of Technology, Kharagpur 721302, West Bengal, India

Manuscript received (revised version): 26 Oct, 1994

model. A numerical or computer simulation of seismic data acquisition can be employed to compute the anticipated seismic response of the model. If, on comparison, the synthetic data closely match with the field-acquired data, the geological interpretation gets verified.

A three-dimensional geological environment may either be reduced to a one- or two-dimensional geophysical representation, depending on the symmetries related to the geological structure and the seismic survey geometry, or it can be simulated in the 3-D space itself.

A comprehensive computer program is required to simulate the physical complexities of wave propagation. A variety of wave types might propagate in the physical environment, viz., *P, SV, SH*, Rayleigh, etc. For the proper selection of a modelling algorithm to simulate these wave types, the characteristics of the medium and the salient features of wave propagation are the most crucial factors.

There are various numerical modelling schemes available to geophysicists, viz., geometrical ray tracing, asymptotic ray theory, generalized ray theory, Fourier synthesis, finite differences, finite elements, etc. Each approach has its own merits and demerits, and is unique in its domain of application.

The finite element method needs faster CPUs, large memory and disc storage to compute and store the enormous volume of data. The present investigation deals with the development of an efficient and economical finite element algorithm for simulating seismic responses in 3-D.

In finite element analysis, generally 'simple' lower order smooth interpolation functions are used to represent the deformation modes. These can be extended to systematic representation of more complex modes through the hierarchy of Legendre's polynomials. Alternatively, the displacement vector at any point for a layered medium can be represented by harmonic expansions in the form of Fourier series. With these ideas in mind, the kinematic condensation of the global matrices is achieved either by introducing hierarchical modes in the form of Legendre's polynomials or by using harmonic expansion in Fourier series [NATH et al. 1990; 1991a, b; 1992; 1993]. The former tackles the problem globally whereas the latter performs better for a layered earth model.

The major features of the proposed kinematic condensations can be summarized as follows:

- Since the CPU requirement is less, the programs can be executed on mini-computers. In fact the present simulation is performed on a HP-9000 series mini-computer.
- At the initial stage of condensation, additional multiplications require extra computational time. But the reduction in the final dimensions of the global matrices cuts down drastically the time required for matrix inversion and also for the subsequent time integration.
- Automatic mesh generation by isoparametric mapping adds generality to the algorithms. Once the software is developed, it is easy to handle a variety of structures and boundary conditions.

— Both the vertical and lateral inhomogeneity and anisotropism can be tackled by controlling the dimensions of the elements.
— Mode of assembly is simple.
— It adds a meaningful interpretation to the analysis in the form of deformation modes.
— Since by the condensation of the deformation modes the degree of freedom is reduced, some of the accuracy is lost though most of it is insignificant because we are interested in the macroscopic response of the subsurface structures.

The inherent disadvantage of these methods is the long execution time even though, compared to the direct finite element method, the total computational time for these condensation algorithms is very low.

At the moment the simulation is performed at the expense of the CPU time in a single array processing environment. Once the parallel processing and computational facility is easily accessible, the kinematic condensation will gain its real entity.

Nomenclature

$U(t)$: displacement vector at any point in the assemblage
U_0 : nodal displacement vector

$\dot{U}(t)$: particle velocity vector

$\ddot{U}(t)$: particle acceleration vector
$\mathbf{M}$: global mass matrix
$\mathbf{K}$: global stiffness matrix
$\mathbf{C}$: global damping matrix
x, y, z: global coordinates
x_e, y_e, z_e: global coordinates at any point in a 3-D solid finite element
$x_{e_i}, y_{e_i}, z_{e_i}$: global coordinates at the i-th node of a 3-D solid finite element
ξ, η, λ: local axes in 3-D space
ξ_i, η_i, λ_i: local coordinates at the i-th node of a 3-D solid finite element
ν: Poisson's ratio
N_i: shape/interpolation function
$N_{i,\xi}$: first derivative of N_i with respect to ξ
$N_{i,\eta}$: first derivative of N_i with respect to η
$N_{i,\lambda}$: first derivative of N_i with respect to λ
u : x-parallel component of displacement vector
v : y-parallel component of displacement vector
w : z-parallel component of displacement vector
$\mathbf{B}$: strain-displacement matrix
$\mathbf{D}$: constitutive matrix
$\mathbf{J}$: Jacobian matrix
$\mathbf{T}$: condensation matrix

$\mathbf{k}_e$, $\mathbf{m}_e$: local stiffness and mass matrices
f_e : local force vector
$\hat{\mathbf{k}}_e$, $\hat{\mathbf{m}}_e$: condensed local stiffness and mass matrices
$\hat{f}_e$: condensed local force vector
α_{ijk}: 3-D global parameter variable

2. General formulation

A general review of the finite element method can be found in many standard texts.

The equation of motion for the displacement vector $U(t)$ may be represented through FEM discretization as,

$$\mathbf{M}\,\ddot{U}(t) + \mathbf{C}\dot{U}(t) + \mathbf{K}U(t) = F(t) \tag{1}$$

where **M, C** and **K** are the global mass, damping and stiffness matrices; $F(t)$ is either an impulsive force or a harmonic loading, and the dot [·] denotes the derivative with time.

The vector $U(t)$ here represents the nodal degrees of freedom at different points in the media. The nodal degrees of freedom may be thought of as discrete values of a continuous function in space and time.

Figures 1, 2 and *3* together represent the geometry of the three-dimensional finite element simulation considering an eight-noded isoparametric solid element. This includes the isoparametric mapping of the global structures, mesh generation, condensation, etc.

Isoparametric mapping and automatic mesh generation

In finite element mesh generation of 3-D surfaces in CAD, ONWUBOLU [1989] has reported the development of a geometric modelling procedure based on a uniform *B*-spline for the representation of general surfaces in 3-D in computer-aided geometric design. The *B*-spline surfaces which are meshes of curves intersecting at model points, facilitate the conversion of the geometric definition into a form compatible with finite element analysis programs. The algorithm converts the *B*-spline surface meshes into six- or eight-noded finite elements.

In order to generate the mesh efficiently, the following points are of vital importance:

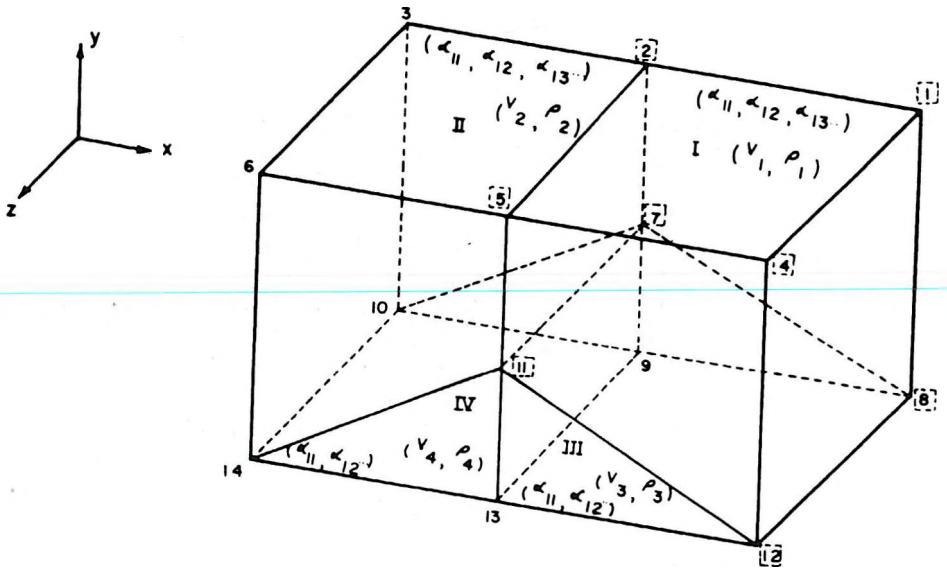

Fig. 1. 3-D global structure
1. ábra. A 3D globális szerkezete

— Continuity across the inter macro-element boundary — thus necessitating equal divisions across the boundaries between neighbouring macro-structures to keep the nodal positions unchanged during discretization.
— To divide each 3-D macro-element into smaller 3-D finite elements for which the global coordinates are to be determined with respect to the key nodal coordinates.

In the present work, we have followed two stages of isoparametric mapping to develop the scheme of discretization by considering trilinear eight-node hexahedron elements.

The isoparametric formulation extends directly from two dimensions to three. We add coordinate z in the global space and a corresponding coordinate λ in the local space and define faces of the element by $\xi, \eta, \lambda = \pm 1$. The isoparametric relationships for an eight-noded solid element can be written as,

$$x_e = \sum_{i=1}^{8} N_i x_{e_i} \; ; \quad y_e = \sum_{i=1}^{8} N_i y_{e_i} \; ; \quad z_e = \sum_{i=1}^{8} N_i z_{e_i} \tag{2}$$

$$u = \sum_{i=1}^{8} N_i u_i \; ; \quad v = \sum_{i=1}^{8} N_i v_i \; ; \quad w = \sum_{i=1}^{8} N_i w_i \tag{3}$$

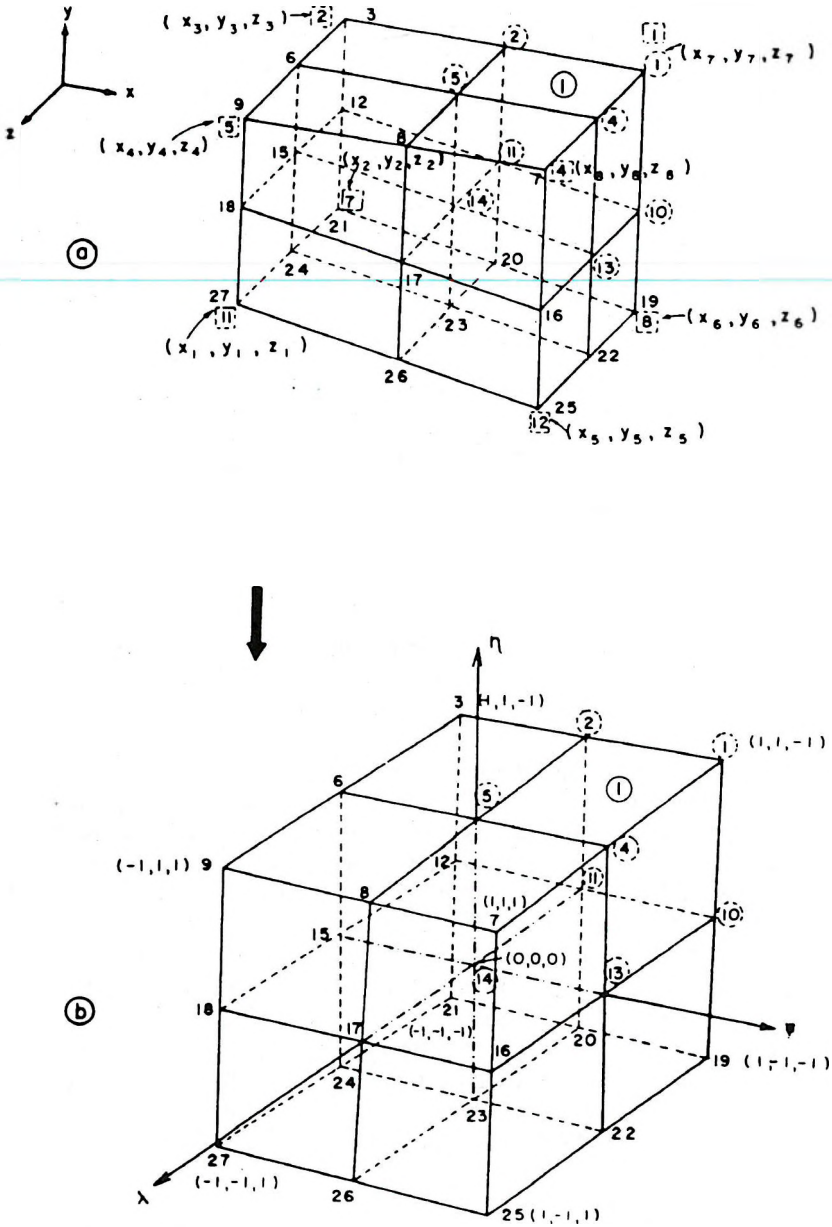

Fig. 2. Finite element discretization, isoparametric mapping and condensation of a 3-D macro-element

2. ábra. Véges elem mintavételezés, egy 3D-s makro elem izoparaméteres leképzése és kondenzációja

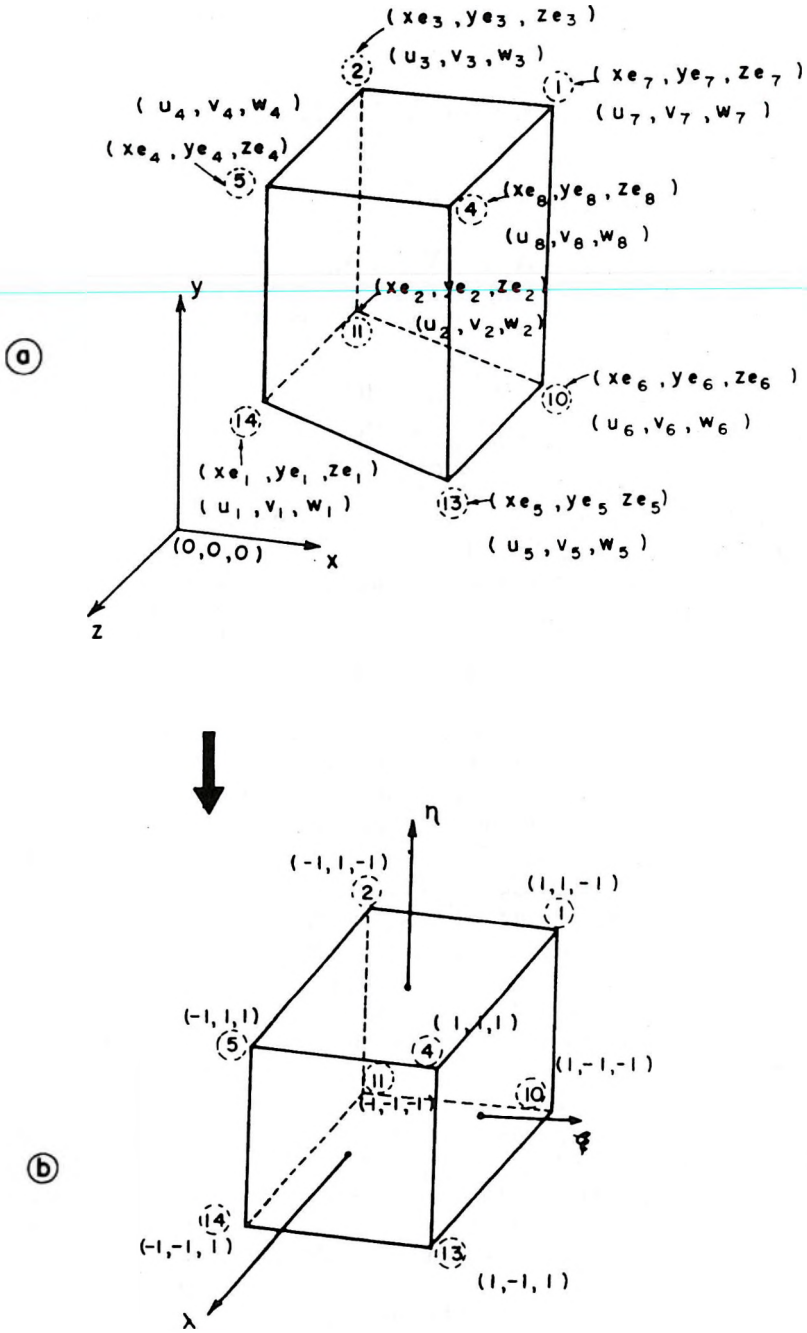

Fig. 3. Isoparametric formulation of an eight-noded solid finite element
3. ábra. Egy nyolc nódusú (csúcsú) véges elem izoparametrikus leírása

where N_i is the three-dimensional interpolation or shape function; it can be given as

$$N_i = \frac{1}{8}(1+\xi\xi_i)(1+\eta\eta_i)(1+\lambda\lambda_i) \quad \text{for } i=1, 2, ..., 8. \tag{4}$$

We define a vector $[\tilde{N}]$ as

$$[\tilde{N}]^T = \{N_1\ N_2\ N_3\ N_4\ N_5\ N_6\ N_7\ N_8\} \tag{5}$$

and the shape function matrix N can be expresssed in terms of the individual shape functions as,

$$\mathbf{N} = \begin{bmatrix} [\tilde{N}]^T & [0] & [0] \\ [0] & [\tilde{N}]^T & [0] \\ [0] & [0] & [\tilde{N}]^T \end{bmatrix} \tag{6}$$

Figure 1 represents a global model subdivided into four macro-structures. Each macro-structure is identified by its density-velocity pair. The macro-level division of the global structure also depends on the change of curvature of the structural boundaries. The *xyz* origin is located at the centroid of the model and *y*, the depth axis is assumed positive upwards [COOK 1974]. The primary nodes with the known coordinates are numbered as shown in Fig. 1.

The discretization of each macro-structure starts with the isoparametric mapping of that individual structure from the *xyz* domain into a local $\xi\eta\lambda$ pace; this is followed by meshing of the mapped structure into a finite number of elements depending on the accuracy and stability requirements for the solution; and, finally, each element of the local space is mapped into the global domain. This is illustrated in Fig. 2a and 2b. Figure 2a represents the macro-structure I of the global model in *xyz* space. The primary global nodes [11], [7], [2], [5], [12], [8], [1] and [4] are the connectivities of macro-structure I with the known coordinates (x_1, y_1, z_1), (x_2, y_2, z_2), (x_3, y_3, z_3), (x_4, y_4, z_4), (x_5, y_5, z_5), (x_6, y_6, z_6), (x_7, y_7, z_7), and (x_8, y_8, z_8), respectively. The right hand rule is strictly followed when numbering the nodes [COOK 1974]. This macro-structure is first mapped into a cubic solid structure in the local $\xi\eta\lambda$ space with the master nodal coordinates (-1, -1, 1), (-1, -1, -1) (-1, 1, -1), (-1, 1, 1), (1, -1, 1), (1, -1, -1), (1, 1, -1) and (1, 1, 1) corresponding to above mentioned global primary nodes [11], [7], [2], [5], [12], [8], [1] and [4] respectively. Depending on the numerical stability of the simulation, the mapped structure in the $\xi\eta\lambda$ space is discretized into a number of eight-noded elements as shown in Fig. 2b. The corner nodes for all the elements are numbered and $\xi\eta\lambda$ coordinates for each node are computed with respect to the master nodes. All the elements are then mapped back into the global domain. For example, element 1 defined by nodes (14), (11), (2), (5), (13), (10), (1) and (4) with the local coordinates $(\xi_1, \eta_1, \lambda_1)$, $(\xi_2, \eta_2, \lambda_2)$, $(\xi_3, \eta_3, \lambda_3)$, $(\xi_4, \eta_4, \lambda_4)$, $(\xi_5, \eta_5, \lambda_5)$, $(\xi_6, \eta_6, \lambda_6)$, $(\xi_7, \eta_7, \lambda_7)$ and $(\xi_8, \eta_8, \lambda_8)$ respectively, when mapped back into the *xyz* domain as shown

in Fig. 2a and represented megascopically in *Fig. 3a*, will have the global coordinates and $(x_{e_1}, y_{e_1}, z_{e_1})$, $(x_{e_2}, y_{e_2}, z_{e_2})$, $(x_{e_3}, y_{e_3}, z_{e_3})$, $(x_{e_4}, y_{e_4}, z_{e_4})$, $(x_{e_5}, y_{e_5}, z_{e_5})$, $(x_{e_6}, y_{e_6}, z_{e_6})$, $(x_{e_7}, y_{e_7}, z_{e_7})$ and $(x_{e_8}, y_{e_8}, z_{e_8})$ respectively. These coordinates can be obtained with respect to the primary nodes and the individual shapes functions as follows:

$$x_{e_i} = \sum_{j=1}^{8} N_{j\,|\,(\xi_i, \eta_i, \lambda_i)}, x_j$$

$$y_{e_i} = \sum_{j=1}^{8} N_{j\,|\,(\xi_i, \eta_i, \lambda_i)}, y_j \qquad (7)$$

$$z_{e_i} = \sum_{j=1}^{8} N_{j\,|\,(\xi_i, \eta_i, \lambda_i)}, z_j \,.$$

The x-parallel, y-parallel and z-parallel components of the displacement vector U_0 at these nodes are (u_1, v_1, w_1), (u_2, v_2, w_2), (u_3, v_3, w_3), (u_4, v_4, w_4), (u_5, v_5, w_5), (u_6, v_6, w_6), (u_7, v_7, w_7), and (u_8, v_8, w_8) respectively.

Once the mesh is generated for the global assemby and the nodal coordinates are computed, each eight-noded element is finally mapped into an isoparametric cubic element as shown in Fig. 3b for the formulation of the element local stiffness and mass matrices.

Element stiffness and mass matrices

The basis expressions for the 3-D element stiffness and mass matrices as formulated from the total strain energy due to internal stresses and the kinetic energy [DESAI, ABEL 1972; COOK 1974; ZIENKIEWICZ 1977] can be given as,

$$\mathbf{k}_e = \iiint \mathbf{B}^T \mathbf{D}\, \mathbf{B}\, dx\, dy\, dz \qquad (8)$$

$$\mathbf{m}_e = \iiint \rho\, \mathbf{N}^T \mathbf{N}\, dx\, dy\, dz \qquad (9)$$

where **B** is the strain-displacement matrix and **D** is the constitutive matrix as defined below.

The constitutive matrix **D**

For an isotropic 3-D body, matrix **D** can be written in terms of Young's modulous E and Poisson's ration ν as

$$\mathbf{D} = \frac{E}{(1+\nu)(1-2\nu)} \begin{bmatrix} (1-\nu) & \nu & \nu & 0 & 0 & 0 \\ \nu & (1-\nu) & \nu & 0 & 0 & 0 \\ \nu & \nu & (1-\nu) & 0 & 0 & 0 \\ 0 & 0 & 0 & 0.5(1-2\nu) & 0 & 0 \\ 0 & 0 & 0 & 0 & 0.5(1-2\nu) & 0 \\ 0 & 0 & 0 & 0 & 0 & 0.5(1-2\nu) \end{bmatrix} \quad (10)$$

Since the finite element method gives a complete solution to the wave propagation, the *P*- and *S*-wave propagation and hence the mode conversion need not be considered separately. The elastic modulus can be computed by considering either the *P*-wave velocity or the shear wave velocity.

Strain-displacement matrix **B**

The strain-displacement matrix **B** cannot be expressed in terms of x, y and z. Hence, we write it in terms of ξ, η and λ. By using only the linear terms of the relations between the strain and the displacement components and by invoking the coordinate transformation of the derivatives, matrix **B** can be written as,

$$\mathbf{B} = \mathbf{H}\,\mathbf{J}^{-1}\,\mathbf{B}_n \quad (11)$$

where,

$$\mathbf{B}_n = \begin{bmatrix} [b] & [0] & [0] \\ [0] & [b] & [0] \\ [0] & [0] & [b] \end{bmatrix} \quad (12)$$

such that

$$[b] = \begin{bmatrix} N_{1,\xi} & N_{2,\xi} & N_{3,\xi} & N_{4,\xi} & N_{5,\xi} & N_{6,\xi} & N_{7,\xi} & N_{8,\xi} \\ N_{1,\eta} & N_{2,\eta} & N_{3,\eta} & N_{4,\eta} & N_{5,\eta} & N_{6,\eta} & N_{7,\eta} & N_{8,\eta} \\ N_{1,\lambda} & N_{2,\lambda} & N_{3,\lambda} & N_{4,\lambda} & N_{5,\lambda} & N_{6,\lambda} & N_{7,\lambda} & N_{8,\lambda} \end{bmatrix} \quad (13)$$

and

$$\mathbf{J}^{-1} = \begin{bmatrix} [J]^{-1} & [0] & [0] \\ [0] & [J]^{-1} & [0] \\ [0] & [0] & [J]^{-1} \end{bmatrix} \quad (14)$$

where **J** is the Jacobian matrix, and,

$$\mathbf{H} = \begin{bmatrix} 1 & 0 & 0 & 0 & 0 & 0 & 0 & 0 & 0 \\ 0 & 0 & 0 & 0 & 1 & 0 & 0 & 0 & 0 \\ 0 & 0 & 0 & 0 & 0 & 0 & 0 & 0 & 1 \\ 0 & 1 & 0 & 1 & 0 & 0 & 0 & 0 & 0 \\ 0 & 0 & 0 & 0 & 0 & 1 & 0 & 1 & 0 \\ 0 & 0 & 1 & 0 & 0 & 0 & 1 & 0 & 0 \end{bmatrix} \tag{15}$$

The stiffness matrix $\mathbf{k}_e$ given by equation (8) can be rewritten in the local domain as,

$$\mathbf{k}_e = \int_{-1}^{+1}\int_{-1}^{+1}\int_{-1}^{+1} \mathbf{B}^T \mathbf{D}\, \mathbf{B}\, |\mathbf{j}|\, d\xi\, d\eta\, d\lambda \tag{16}$$

The above expression for $\mathbf{k}_e$ must be evaluated numerically by writing it in the summation form as

$$\mathbf{k}_e = \sum_{i=1}^{n_g}\sum_{k=1}^{n_g}\sum_{m=1}^{n_g} \mathbf{B}^T \mathbf{D}\, \mathbf{B}\, |j|\, \omega_i\, \omega_k\, \omega_m \tag{17}$$

Similarly, mass matrix $\mathbf{m}_e$ given by equation (9) can be expressed in the summation form:

$$\mathbf{m}_e = \sum_{i=1}^{n_g}\sum_{k=1}^{n_g}\sum_{m=1}^{n_g} \rho\, \mathbf{N}^T \mathbf{N}\, |j|\, \omega_i\, \omega_k\, \omega_m \tag{18}$$

where n_g is the number of Gauss points in the solid element, ω_i, ω_k, ω_m are the weighting functions at these Gauss points (n_g, ω_i, ω_k and ω_m are obtained from standard tables).

Condensation and time integration

Let $u\ (x,t)$ be a continuous function which represents the actual displacement of a point in the domain concerned. Then we can write,

$$U(X_i, t) = u\ (x=X_i, t) \tag{19}$$

This continuous function u may further be expanded in terms of a Fourier series as

$$u(x, t) = \sum_n \alpha_n f_n(x) \tag{20}$$

where $\alpha_n(t)$ are the time dependent generalized Fourier coefficients and $f_n(x)$ are the Fourier expansions in space coordinates.

The above equation may be put in the matrix form, viz.

$$u(x, t) = \boldsymbol{p}^T(x)\, \alpha(t) \tag{21}$$

where

$$\boldsymbol{p}^T(x) = (f_0(x)\ f_1(x) \ldots f_n(x))$$

$$\alpha^T(t) = (\alpha_0(t)\ \ \alpha_1(t) \ldots \alpha_n(t))$$

Using the above notations, displacement at a discrete point X_i is represented as

$$\boldsymbol{U}_i(X_i, t) = \boldsymbol{p}^T(X_i)\, \alpha(t) \tag{22}$$

where $\boldsymbol{U}_t(X_i, t)$ is the displacement vector at point X_i at any time instant t.

In the above treatment the following points must be noted:

— although $f_n(x)$ are orthogonal in function space, components $p(X_i)$ are not continuous and represent the discrete value of $f_n(x)$ at point X_i; hence $\boldsymbol{p} \times \boldsymbol{p}^T$ is not a diagonal matrix.

— relationship (21) is a Fourier expansion but transformation (22) is simply a discrete representation.

The displacement vector $\boldsymbol{U}$ at any node can be further written as

$$\boldsymbol{U} = \begin{bmatrix} u \\ v \\ w \end{bmatrix} \tag{23}$$

Using relations (19) and (20), equation (23) can be approixmated by rolling independent Legendre's polynomials in the x, y and z directions. The terms u, v and w can be expanded by Legendre's polynomials:

$$u = \sum_{i=0}^{n} \sum_{j=0}^{m} \sum_{k=0}^{l} \alpha_{ijk}\, P_i(x)\, P_j(y)\, P_k(z) \tag{24}$$

$$v = \sum_{i=0}^{n} \sum_{j=0}^{m} \sum_{k=0}^{l} \alpha_{(i+nml)\,(j+nml)\,(k+nml)}\, P_i(x)\, P_j(y)\, P_k(z) \tag{25}$$

$$w = \sum_{i=0}^{n} \sum_{j=0}^{m} \sum_{k=0}^{l} \alpha_{(i+2nml)\,(j+2nml)\,(k+2nml)}\, P_i(x)\, P_j(y)\, P_k(z) \tag{26}$$

In the above equations α is the global parameter matrix in 3-D for the global structure shown in Fig. 1, and $P_i(x)$, $P_j(y)$, $P_k(z)$ are the associated Legendre's polynomials in the x, y and z directions respectively.

Hence, relationship (23) takes the form,

$$\boldsymbol{U} = \mathbf{T}\,\alpha \tag{27}$$

where T is the condensation matrix. Using expressions (24), (25) and (26) and considering element 1 of Fig. 3, we can define a matrix $[\tilde{t}]$ such that

$$[\tilde{t}] = \begin{bmatrix} P_0(x_{e_1}) & P_0(y_{e_1}) & P_0(z_{e_1}) & P_0(x_{e_1}) & P_0(y_{e_1}) & P_1(z_{e_1}) & \cdots \\ P_0(x_{e_2}) & P_0(y_{e_2}) & P_0(z_{e_2}) & P_0(x_{e_2}) & P_0(y_{e_2}) & P_1(z_{e_2}) & \cdots \\ & \cdots & & & \cdots & & \cdots \\ P_0(x_{e_7}) & P_0(y_{e_7}) & P_0(z_{e_7}) & P_0(x_{e_7}) & P_0(y_{e_7}) & P_1(z_{e_7}) & \cdots \\ P_0(x_{e_8}) & P_0(y_{e_8}) & P_0(z_{e_8}) & P_0(x_{e_8}) & P_0(y_{e_8}) & P_1(z_{e_8}) & \cdots \end{bmatrix} \tag{28}$$

then the element condensation matrix T can be written as

$$\mathbf{T} = \begin{bmatrix} [\tilde{t}] & [0] & [0] \\ [0] & [\tilde{t}] & [0] \\ [0] & [0] & [\tilde{t}] \end{bmatrix} \tag{29}$$

Now considering the element static equilibrium equation when subjected to an external force vector f_e and substituting relationship (27) for the displacement vector $\boldsymbol{U}$, we can write,

$$\mathbf{k}_e\,\mathbf{T}\,\alpha = f_e \tag{30}$$

Premultiplying both sides of equation (30) by $\mathbf{T}^T$ we get,

$$(\mathbf{T}^T\,\mathbf{k}_e\,\mathbf{T})\,\alpha = \mathbf{T}^T f_e \tag{31}$$

By the same token, the element dynamic equilibrium equation with damping neglected can be written as

$$(\mathbf{T}^T\,\mathbf{m}_e\mathbf{T})\,\ddot{\alpha} + (\mathbf{T}^T\,\mathbf{k}_e\mathbf{T})\,\dot{\alpha} = \mathbf{T}^T f_e \tag{32}$$

Since, by condensation, the degree of freedom is reduced, $\mathbf{T}^T$ will reduce the number of equations and at the same time will condense the local stiffness and mass matrices into the symmetric global matrices. $\mathbf{T}^T$ will transform the local force vector or the array of local force vectors into an equivalent condensed global force vector or an array of force vectors.

The condensation matrix **T** transforms the element stiffness matrix $\mathbf{k}_e$ into $\hat{\mathbf{k}}_e$, mass matrix $\mathbf{m}_e$ into $\hat{\mathbf{m}}_e$ and the array of external force vectors f_e into $\hat{f}_e$ such that

$$\hat{\mathbf{k}}_e = \mathbf{T}^T \mathbf{k}_e \mathbf{T} \tag{33}$$

$$\hat{\mathbf{m}}_e = \mathbf{T}^T \mathbf{m}_e \mathbf{T} \tag{34}$$

$$\hat{f}_e = \mathbf{T}^T f_e \tag{35}$$

These matrices are then assembled by direct addition into the corresponding global matrices **K**, **M** and **F**. The stiffness and mass matrices of all the basement elements are first compacted before condensing and assembling.

The dimensions of **K** and **M** will be $(n \times n)$ where

n = 3 × no. of polynomials in the x direction
× no. of polynomials in the y direction
× no. of polynomials in the z direction

It is difficult to assess the global matrix **C**. Actually it should be determined from the attenuation of the waves obtained from the field records. However, common practice assumes the **C** matrix to be proportional to mass **M** and the stiffness **K** matrices. For example, $\mathbf{C} = \beta\mathbf{M} + \gamma\mathbf{K}$, where β and γ are the proportionality constans.

The equilibrium equation of motion (1) in 3-D thus gets converted into the second order differential equation in α. This equation is then transformed into the following form (36) by the central difference method and is solved by direct integration or by mode superposition and Cholesky decomposition [BATHE, WILSON 1976] after initiating the wavefield and introducing boundary conditions:

$$\alpha_{|(t+\Delta t)}\left(\frac{\mathbf{M}}{\Delta t^2} + \frac{\mathbf{C}}{2\Delta t}\right) = \mathbf{F}(t) - \left(\mathbf{K} - 2\frac{\mathbf{M}}{\Delta t^2}\right)\alpha_{|(t)} - \left(\frac{\mathbf{M}}{\Delta t^2} - \frac{\mathbf{C}}{2\Delta t}\right)\alpha_{|(t-\Delta t)} \tag{36}$$

where 'Δt' is the sampling interval and 't' is the instant of time at which the response is computed.

Since **U** is a function of α, x, y and z, on solving for α **U** is calculated which, on differentiation by the central difference method, gives the particle velocity vector and hence the seismic response at a particular node.

Boundary conditions

The boundary conditions specified here are as follows:

— At the bottom, the boundary is taken to be rigid, though apparently this may give rise to a standing wave in the strata. However, the bottom boundary

should be lowered enough so that the reflections from this do not intermingle with the actual seismic events and thus the salient features are brought out in the numerical results.

— The side boundaries are taken as free so that they do not produce a confining effect. In this case the oblique incident waves will split and reverse their sign. But this is of no major consequence in a practical case where the horizontal extent of the boundary is much greater than its depth. Hence at least in the middle portion of the model the seismogram represents an undistorted picture of the reflected waves.

It is possible to incorporate absorbing boundary conditions for the edges [KEYS 1985]. However, in the present simulation we do not fint it to have any pronounced effect.

3. Numerical model study

In order to carry out an ideal synthetic 3-D survey, one can compute a large number of shot records for each profile on the simulated earth surface, do the normal moveout corrections and further processing in order to obtain stack sections for all the seismic lines. This involves an extensive amount of computational effort. But a normal incidence seismogram constructed by placing the source at a grid location on the surface and computing the seismic response at that grid position only and then shifting the source-receiver position to the next grid location and so on, resembles an actual unmigrated CDP time section.

In selecting a 3-D modelling example, MUFTI [1990] suggested the following points:

— as far as possible the model should be based on and represent real geology,

— the model should be characterized by prominent 3-D structural features,

— to interpret the seismic results easily, the model should be as simple as possible.

With the above aspects in mind, we have performed the following numerical simulation of a 3-D dome model in order to test the effectiveness of the three-dimensional modelling algorithm discussed in the previous sections.

3-D dome model

A finite element three-dimensional model is set up by considering a dome structure as shown in *Fig. 4* generated by a 3-D cubic *B*-spline program. It extends both east-west and northsouth to 2 km. The depth extent is set to 1 km

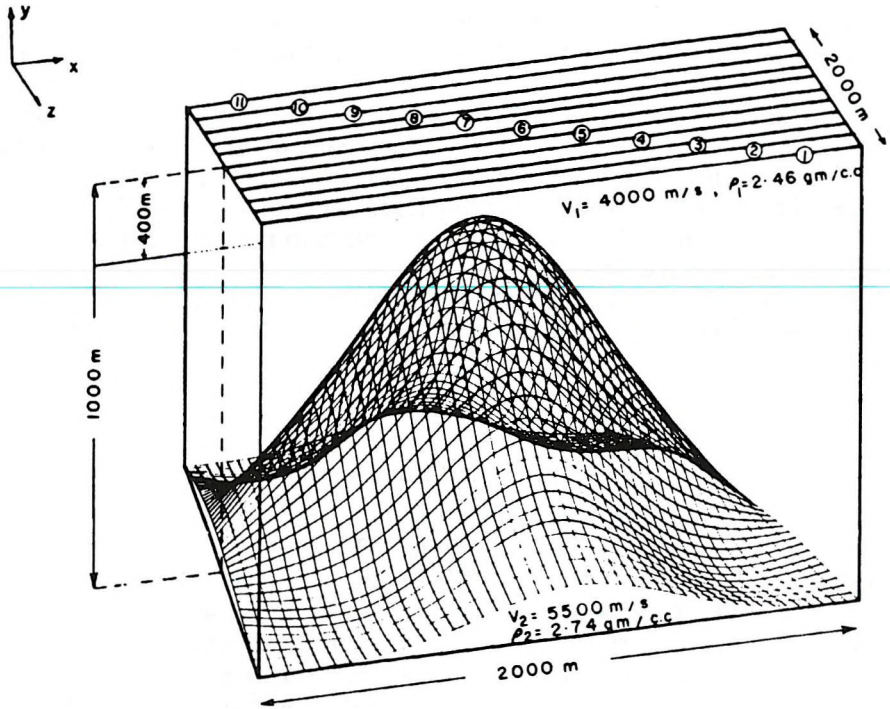

Fig. 4. A 3-D dome structure (2 km × 1 km × 2 km) — Configuration and physical parameters
4. ábra. 3D-s dóm szerkezet (2 km × 1km × 2km) — elrendezés és a fizikai paraméterek

with the top of the hump at 400 m from the horizontal plane of observation. The top surface layer has a density of 2.46 gm/cm^3 and a *P*-wave propagation velocity of 4000 m/s. The compact base layer has a *P*-wave propagation velocity of 5500 m/s and a density of 2.74 gm/cm^3. *Figure 9* represents the depth contour map at 50 m interval over the dome model. This diagram is the two-dimensional geometrical representation of the 3-D model of Fig. 4. The 500 m contour in this diagram represents the proximity of the top of the dome formation, the bottom of it is represented by the 1000 m contour. For stiffness computation, Poisson's ratio was taken as 0.25.

The starting point of the 3-D simulation of the above model is the macro-level discretization of the entire global structure depending on the change of curvature of the dome interface. As presented in *Fig. 5*, this model is first subdivided into 32 solid eight-noded macro-elements bounded by 71 principal nodal points. Each solid macro-element is in turn isoparametrically mapped and discretized into 1000 finite elements. Thus, the whole global model is isoparametrically disseminated into 32,000 finite elements. Although the accuracy of the seismogram depends on the size of the element or the mesh size used in the discretization of the structure, we had to restrict ourselves to

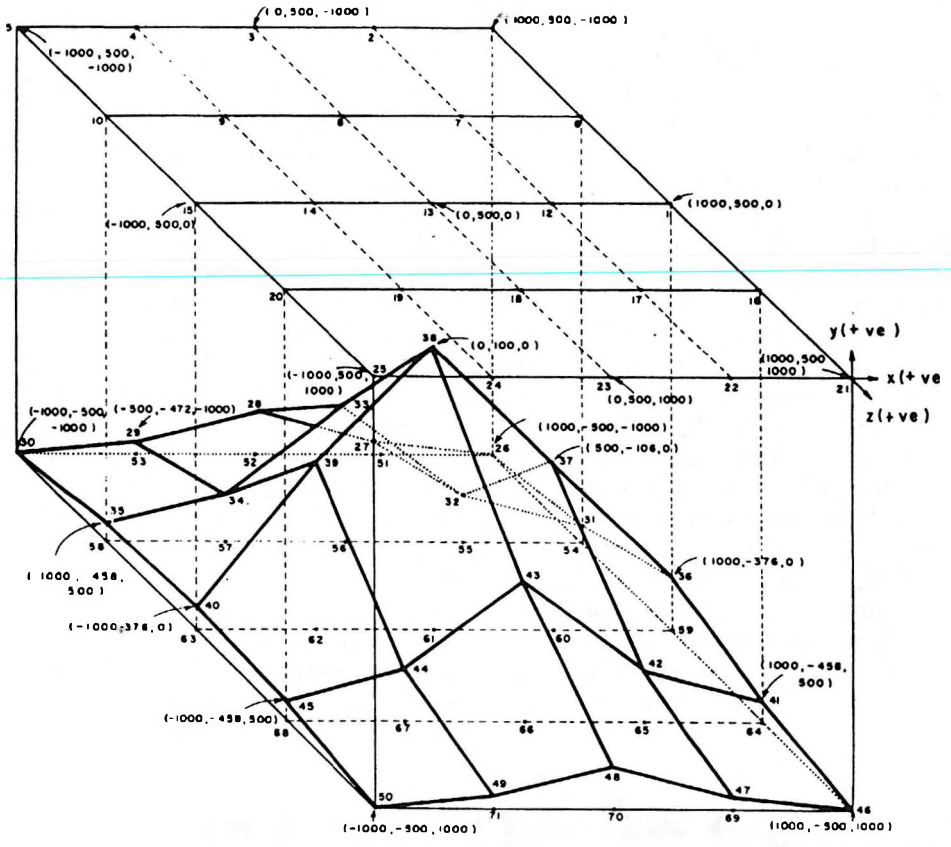

Fig. 5. Macro-level discretization of the 3-D dome model of Fig. 4.
5. ábra. A 4. ábrán látható 3D-s modell makro szintű mintavételezése

only 32,000 elements — which is slightly coarser than would have been necessary for a 0.5 ms sampling interval as per the numerical stability criteria.

A synthetic 3-D survey is conducted by dividing the observation plane into 11 x-parallel profiles. Each profile from our 3-D data volume represents a seismic line along which the geologic model resembles, as closely as possible, a 2-D structure. All the 11 profiles on the surface are drawn and marked in Fig. 4. Each seismic line is assigned 55 trace/source-receiver locations. An external load of 10,000 N acting for one sample duration is used to simulate the 3-D array of impulsive force vectors. The normal incidence synthetic seismic responses are computed for 11×55 grid locations at 0.5 ms sampling rate. Time integration is performed for a total of 1500 time steps.

Seismograms along profiles 1 to 6 as depicted in Figs. 6 to 8 together present the gradual change of the curvature of the relection pattern from the

dome interface as the structure is tracked from the flank to the top. *Figure 6a* shows the seismic section modelled along profile 1. The strong event '*A*' at 420 ms to 450 ms between traces 28-1 and 28-55 is from the relatively flattened section of the dome. This event '*A*' gains curvature when modelled along profile 2 as shown in *Fig. 6b*. The modelling response of the dome interface in this section is located at 360 ms to 450 ms between traces 28-1 and symmetrically between traces 28-55. The dome structure becomes more prominent when modelled along profile 3 as is evident from the normal incidence synthetic time section of *Fig. 7a*. Reflection event '*A*' can be detected at 330 ms to 450 ms between the source-receiver positions 28-1 and symmetrically between 28-55. When simulated along profile 4, the synthetic zero-offset time section presented in *Fig. 7b,* represents the strong reflection event '*A*' at 270 ms to 450 ms between the surface positions 28-1 and 28-55. The same event 'A' appears at 240 ms to 450 ms between traces 28-1 and symmetrically between traces 28-55, while modelling responses from the dome are computed along seismic line 5 as shown in *Fig. 8a*. Profile 6 is at the mid surface location and the entire model is symmetrically divided along this profile only. When the 3-D simulation is performed along this line, reflection event '*A*' from the dome gains the maximum curvature as is depicted in *Fig. 8b*. In this zero-offset section, seismic event '*A*' can be detected at 230 ms to 450 ms between traces 28-1 and symmetrically between locations 28-55.

In all six zero-offset sections, one can identify an out-of-plane event '*B*' just above the reflections arrivals from the dome interface. In the section along profile 1 of Fig. 6a, event '*B*' is quite prominent and is located at 210 ms to

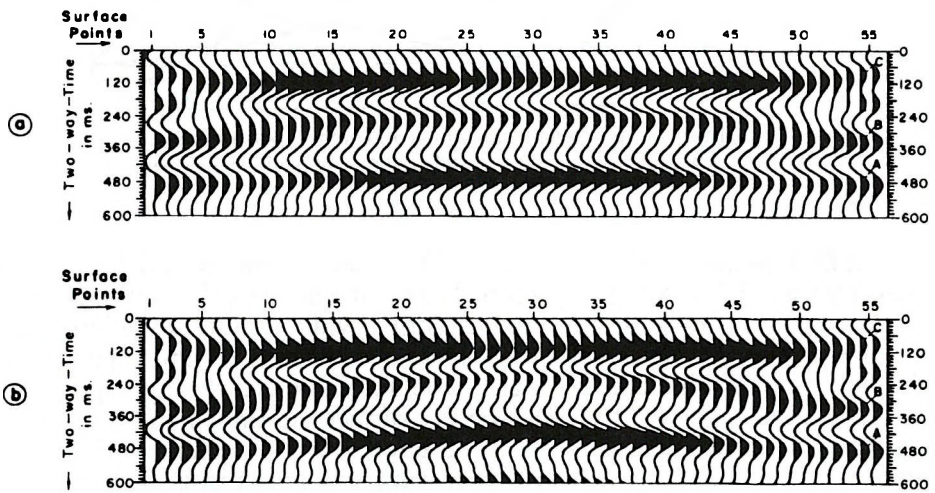

Fig. 6. Normal incidence synthetic time section along: (a) Profile 1; (b) Profile 2
6. ábra. Merőleges beesésű szintetikus időszelvény. (a) 1. szelvény; (b) 2. szelvény

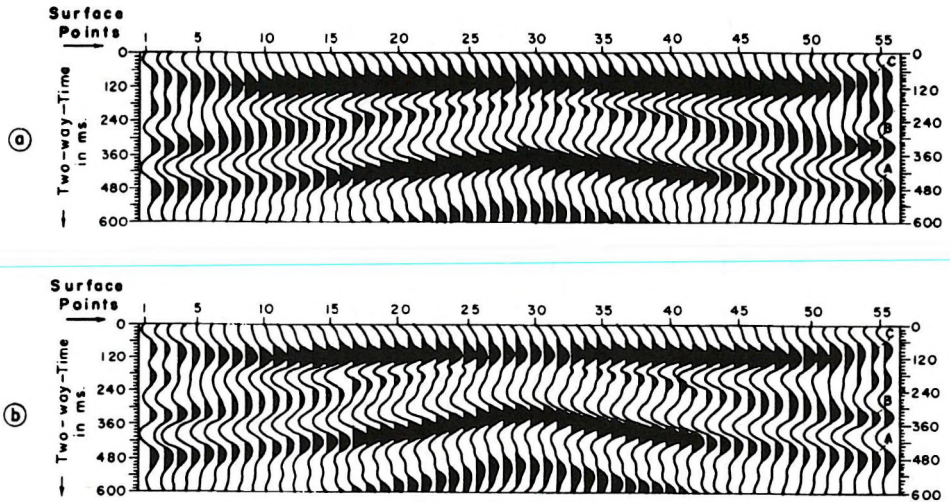

Fig. 7. Normal incidence synthetic time section along: (a) Profile 3; (b) Profile 4
7. ábra. Merőleges beesésű szintetikus időszelvény: (a) 3. szelvény; (b) 4. szelvény

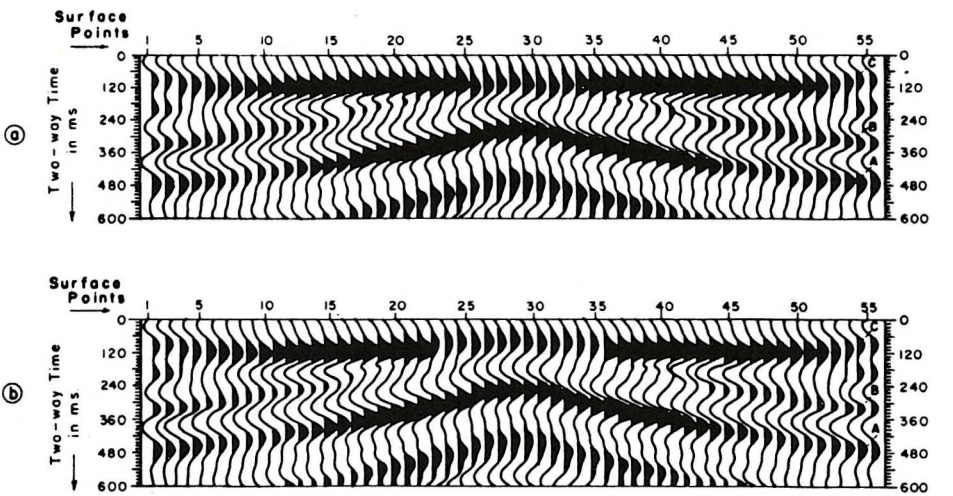

Fig. 8. Normal incidence synthetic time section along: (a) Profile 5; (b) Profile 6
8. ábra. Merőleges beesésű szintetikus időszelvény: (a) 5. szelvény; (b) 6. szelvény

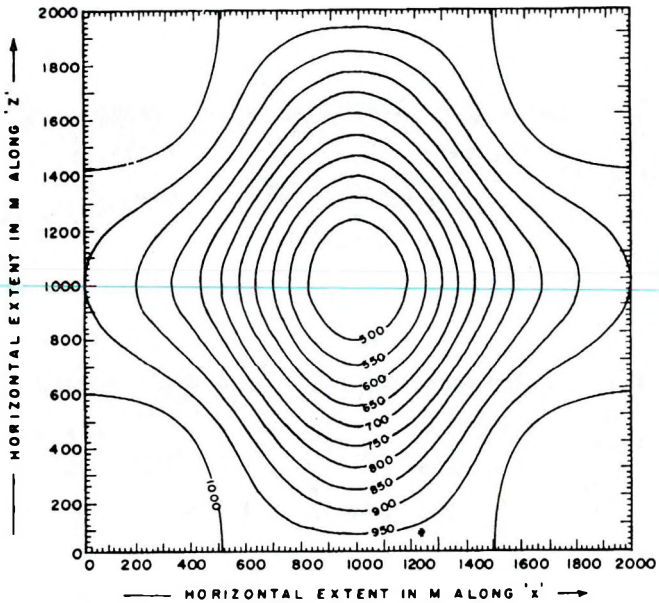

Fig. 9. Depth contour map over the 3-D dome model
9. ábra. A 3D dóm modell mélységtérképe

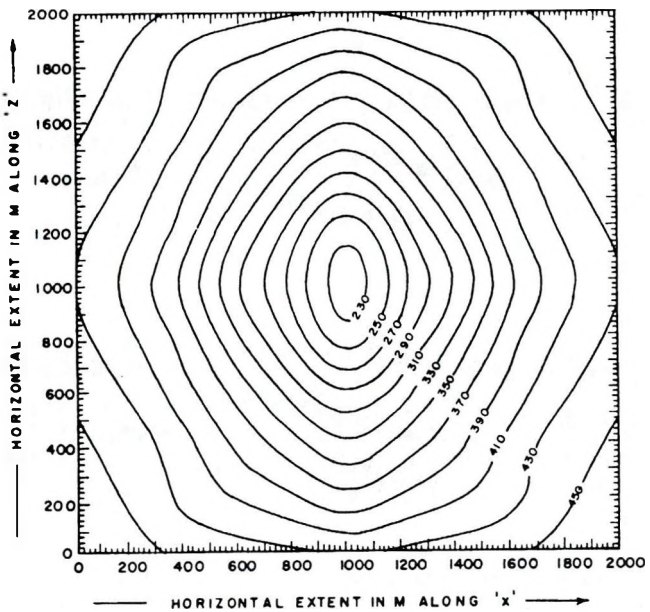

Fig. 10. Simulated isotime map over the 3-D dome model
10. ábra. A 3D dóm modell szimulált időtérképe

300 ms between traces 28-1 and traces 28-55. Event '*B*' becomes feeble and weaker as the central profile is approached. In the section along proflie 3, the amplitude of event '*B*' is very low. In the seismogram along line 4, this event is absent between trace locations 28-25 and 28-31. In the time section along profile 5, event 'B' is totally absent between locations 22-28 and 28-34, and at other locations the amplitude is extremely low. Normal incidence synthetic seismogram along the central profile 6, contains only a faint trace of event '*B*' at the source-receiver positions 1 to 19 and 37 to 55. Seismic event '*B*' can be attributed to the interference of the side reflections from the dome.

Near the top of all the seismic sections of all the profiles, a comparatively flat event '*C*' is observed. This event is due to the first compressions on the arrival of the direct wave because of the external impact.

In the zero-offset sections along profiles 2, 3, 4, 5 and 6, an event is noticed at the base of each seismogram. This event is due to the multiple reflections.

The seismograms of profiles 7-11 are the mirror images of profiles 1-5.

Although the reflection event is somewhat stronger in all the sections, the overall frequency content seems to be lower. In order to make an estimate of the frequency content in the synthetic time sections, FFT is run on trace 28 of profile 6. The resulting amplitude spectrum is presented in *Fig. 11.* This spectrum shows a freqency range of about 0-72 Hz with 38 Hz being the most dominant one.

By making a qualitative analysis of all the sections along the seismic profiles just discussed, one can thus identify all the in-plane and out-of-plane events by differentiating between the consistency of the pulse signatures. Further insight about the nature of seismic events can be gained by identifying them in the time slices, and how they vary areally as a functions of time. Representative time slices are presented in Figs. 12 to 15 for 200 ms, 300 ms, 400 ms and 500 ms respectively.

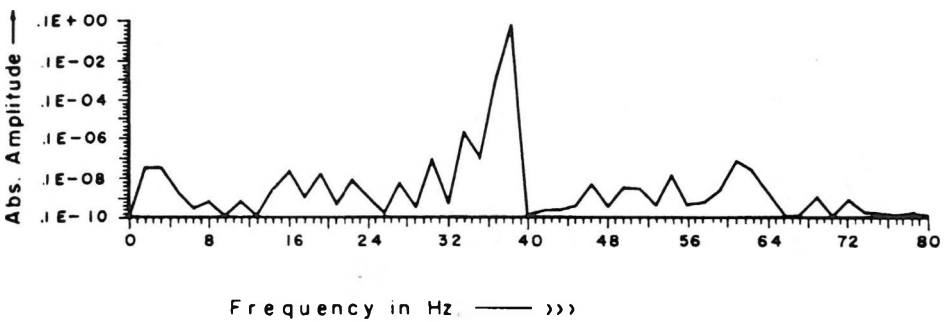

Fig. 11. Amplitude spectrum of trace 28 of profile 6
11. ábra. A 6. szelvény 28. csatornájának amplitúdó spektruma

Figure 12 shows the time slice for 200 ms in grey level with the intensity varying gradually between the dark representing a minimum amplitude of -0.70E-05 to the bright representing a maximum value of 0.27E-05. The brightest band appearing at the flanks of the diagram is due to the interferences of the side reflections. The bright band reappears in patches at the central region. This is the out-of-plane event. The time slice for 300 ms is given in *Fig. 13.* The central bright image corresponding to a maximum value of 0.59E-05 represents reflection event '*A*'. This image increases in dimensions in the next time slice for 400 ms in *Fig. 14.* In *Fig. 15.* we get the multiple effect. In all the time slices the same grey look-up table is used.

In the next phase of the simulation, the time of arrival for each reflection signal at all the 11×55 positions is picked up and an isotime map at 20 ms contour interval is prepared over the 3-D dome model. The time contour map thus simulated is presented in Fig. 10 with the innermost contour labelled 230 ms and the outer-most one labelled 450 ms. The depth contour map presented in *Fig. 9* shows a close match with the synthetic isotime map of Fig. 10 thus justifying the validity of the proposed numerical modelling algorithm.

In the above algorithm, 3-D condensation of the local matrices is achieved by using 10 hierarchical modes.

The result of the numerical model example presented above demonstrate that wavefields for meaningfully sized 3-D models of interest to exploration geophysicists can be computed using the 3-D Finite Element Legendre Polynomial Condensation Technique on mini-computers. The main advantage of this algorithm lies in its generality in automatic meshing and its capability in tackling both the latereal and vertical inhomogeneities.

4. Conclusion

Much of the current methodology of seismic data processing is based on the assumption that the earth can be adequately represented by a horizontally stratified medium. Over the years, this simiplistic picture of the subsurface has influenced our attitude and style of thought regarding the nature of seismic data. But the above algorithm simulates the wavefield by assigning global parameter variables to the entire model.

All the published forward modelling algorithms vary greatly in accuracy and model generalization. It is well known that both the finite-difference and finite element formulations are more efficient than the Fourier and other methods. The method of condensation as envisaged in the present study adds further efficiency to the finite element modelling scheme. The probable source of error that might be associated with this algorithm is due to the spatial discretization and time integration as restricted in parts by the considerable computer storage and speed that are necessary. If the mesh size and the time step increments are coarser, the simulated seismic sections will be devoid of higher frequency components. The recent advances in computer technology

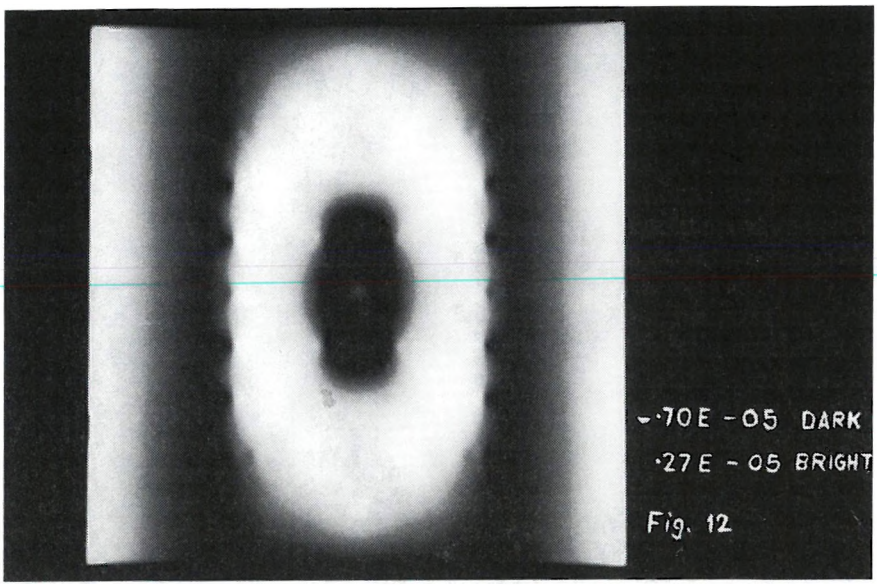

Fig. 12. Time slice for 200 ms
12. ábra. 200 ms-os időmetszet

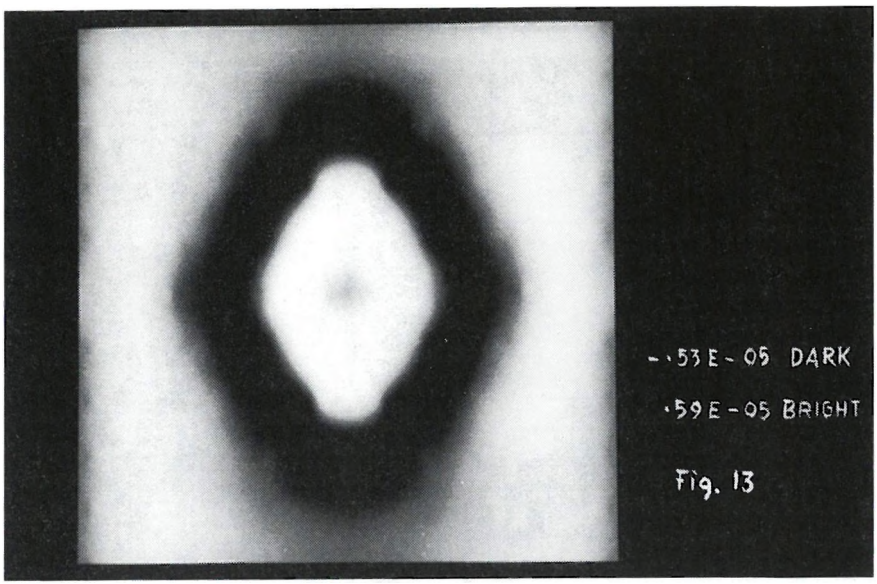

Fig. 13. Time slice for 300 ms
13. ábra. 300 ms-os időmetszet

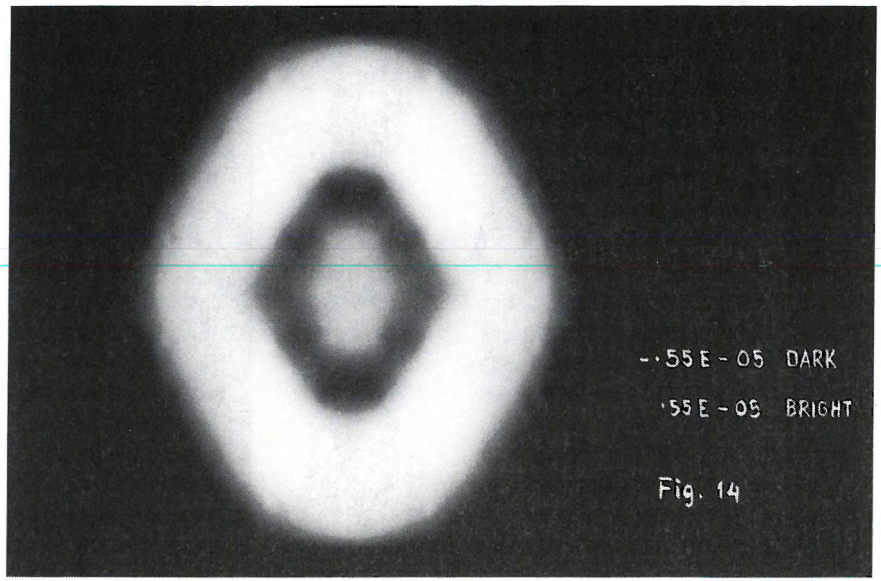

Fig. 14. Time slice for 400 ms
14. ábra. 400 ms-os időmetszet

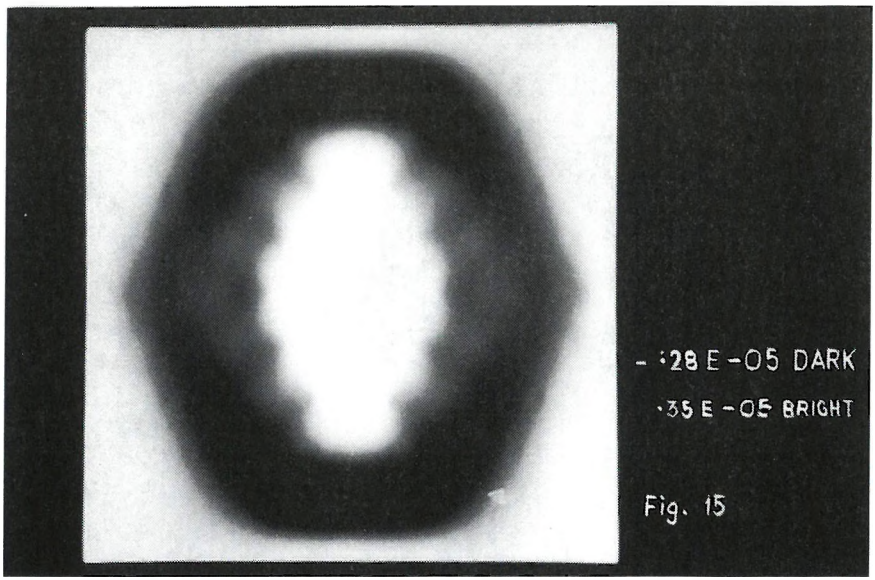

Fig. 15. Time slice for 500 ms
15. ábra. 500 ms-os időmetszet

— especially the size of fast, accessible memory, however — have the greatest impact on this 3-D forward modelling scheme.

The efficacy of the method has been tested on a three-dimensional dome shaped structure having a velocity of 5500 m/s and density 2.74 gm/cm^3 overlain by a top layer of velocity 4000 m/s and density 2.46 gm/cm^3. The model is subdivided into 32,000 elements and normal incidence synthetic seismic responses are computed for 11×55 grid locations at 0.5 ms sampling rate for a total of 1500 time steps. By making a qualitative analysis of all the time sections we can identify all the in-plane and out-of-plane events. Further insight regarding the nature of seismic events is obtained after the amplitudes are displayed as raster images in time slices and their variation with time. The isotime map prepared from the reflected arrivals also finds a good match with the depth contour map thus establishing the validity of this condensation technique.

REFERENCES

BATHE K. J., WILSON E. L. 1976: Numerical Methods in Finite Element Analysis. Prentice - Hall, Englewood Cliffs, USA

COOK R. D. 1974: Concepts and Application of Finite Element Analysis. John Wiley and Sons, New York

DESAI C. S., ABEL J. F. 1972: Introduction to Finite Element Method - a Numerical method for engineering analysis. Litton Educational Publishing, New York

KEYS R. G. 1985: Absorbing boundary conditions for acoustic media. Geophysics **50**, pp. 892-902

LOEWENTHAL D., LU L., ROBERTSON R., SHERWOOD J. 1976: The wave equation applied to migration. Geophysical Prospecting **24**, pp. 380-399

MUFTI L. R. 1990: Large Scale Three-Dimensional Seismic Models and their Interpretive Significance. Geophysics **55**, pp. 1166-1182

NATH S. K., MAJUMDAR S., SENGUPTA S. 1990: Simulation of Seismic Responses by Finite Element Condensation. Paper No. MC-30, presented at the 35th Congress of ISTAM

NATH S. K., MAJUMDAR S., SENGUPTA S. 1991a: Finite Element Condensation technique in modelling normal incidence synthetic seismograms. Indian Journal of Geology **63**(1), pp. 6-16

NATH S. K., MAJUMDAR S., SENGUPTA S. 1991b: Synthetic seismograms by finite element condensation technique for two dimensional geological structures. Journal of Association of exploration Geophysicists **XII** (1), pp. 45-54

NATH S. K., MAJUMDAR S., SENGUPTA S. 1992: Two Dimensional Seismic Modelling by Finite Element Legendre Polynomial Condensation. Bollettino de Geofisica Teorica ed Applicata **XXXIV**, pp. 03-19

NATH S. K., MAJUMDAR S., SENGUPTA S. 1993: Finite Element Simulation of Two-Dimensional Seismic Wave Propagation. Computers and Structures **49**, pp. 97-106

ONWUBOLU G. C. 1989: Finite Element Mesh Generation of 3-D Surface in CAD. Computers and Structures **32**, pp. 31-36

ZIENKIEWICZ O. C. 1977: The Finite Element Method. 3rd expanded and revised edition, McGraw-Hill, London

HÁROMDIMENZIÓS SZEIZMIKUS MODELLEZÉS VÉGES ELEMES KONDENZÁCIÓS MÓDSZERREL

Sankar Kumar NATH, Swapan MAJUMDAR and Saradindu SENGUPTA

Egy szeizmikus szelvény a háromdimenziós térben terjedő reflektált hullám kétdimenziós képe. A mai számítástechnikai eszközök lehetővé teszik a rétegsor szeizmikus válaszának sokkal pontosabb vizsgálatát, ha a hullámegyenleteket 3D-s modellekre írjuk fel. Számos olyan numerikus modellezési eljárás alkalmas a 3D-s szeizmikus válaszfüggvény szimulációjára, mint amilyen a véges elemes eljárás is. Más sémákhoz képest ez az eljárás a számítógépek hatékony hálózatát igényli a többszörös fedésű rendszerek kezeléséhez. E dolgozat célja egy gazdaságos és jó hatásfokú véges elemes algoritmust adni a 3D-s szeizmikus modellezéshez, amely szem előtt tartja: (i) a memória és tárolási kapacitás csökkentését, (ii) az alkalmazhatóságot multiprocesszorork és mini-számító gépek esetén. Ahhoz, hogy a szabadságfok mértéke csökkenthető legyen egymás alá- és fölérendelési (hierarchikus) módokat vezettek be a Legendre polinómokban, és ezzel elérik a globális mátrixok kinematikus kondenzációját. Hat vonal mentén számoltak ki merőleges beesésű szintetikus szeizmogramot egy 3D-s dóm modell felett. Az eredmények pillanatnyi időmetszetével és izovonalas időtérképekkel igazolják a javasolt algoritmus értékét.